Highlights

Physics-informed Neural Network Combined with Characteristic-Based Split for Solving Navier-Stokes Equations

Shuang Hu,Meiqin Liu,Senlin Zhang,Shanling Dong,Ronghao Zheng

- This method disregards the weights between output parameters.

- This method is a rapid version of Physics-informed Neural Network, as not all partial derivatives are involved in the gradient backpropagation, and the remaining terms are reused.

- This method can solve Shallow-Water equations and incompressible N-S equations.

- This method only requires the flow field information at a specific time to reconstruct the flow field information from both the past and future.

Physics-informed Neural Network Combined with Characteristic-Based Split for Solving Navier-Stokes Equations[⋆]

Shuang Hu[a,b], Meiqin Liu[c,a,∗,1], Senlin Zhang[a,b], Shanling Dong[a,b] and Ronghao Zheng[a,b]

[a]*College of Electrical Engineering, Zhejiang University, Hangzhou, 310027, China*

[b]*State Key Laboratory of Industrial Control Technology, Zhejiang University, Hangzhou, 310027, China*

[c]*Institute of Artificial Intelligence and Robotics, Xi'an Jiaotong University, Xi'an, 710049, China*

ARTICLE INFO

Keywords:
Physics-informed Neural Network
Characteristic-based split algorithm
partial differential equations
Navier-Stokes equations

ABSTRACT

In this paper, we propose a physics-informed neural network (PINN) combined with characteristic-based split (CBS) method for solving time-dependent Navier-Stokes equations (N-S equations). The proposed method separates the output parameters and corresponding losses, thereby disregarding weights between output parameters. Additionally, not all partial derivatives participate in gradient backpropagation, allowing for the reuse of remaining terms. As a result, this method is a faster version than traditional PINN. The labeled data, physical constraints, and network outputs are considered as priori information, and the residuals of the N-S equations are treated as posteriori information. This approach enables the handling of both data-driven and data-free problems. Notably, the method can solve the compressible N-S equations, specifically the Shallow-Water equations, and incompressible N-S equations. Given the known boundary conditions, the method requires only flow field information at a specific time to restore past and future flow field information. We demonstrate the potential of this method in marine engineering by solving the progress of a solitary wave onto a shelving beach and the dispersion of hot water in the flow. Furthermore, we prove the correctness and universality of the method by solving incompressible N-S equations with exact solutions. The source codes for the numerical examples in this work are available at `https://github.com/double110/PINN-cbs-.git`.

1. Introduction

Partial differential equations (PDEs) are mathematical equations that involve functions of multiple variables and their partial derivatives. They describe many physical phenomena, including the flow of fluids, the propagation of sound and light waves, and the diffusion of heat. PDEs are used extensively in physics, engineering, and other sciences to model complex systems and analyze their behavior. The methods for solving PDEs based on neural networks are mostly data-driven. When there is sufficient spatiotemporal scattered point measurement data or the exact solution is known, using neural networks to solve computational fluid dynamics (CFD)-related problems such as parameter estimation, flow field reconstruction, and proxy model construction shows great potential. Long, Lu, Ma and Dong (2018); Long, Lu and Dong (2019) proposed a feedforward neural network (PDE-Net) to invert unknown PDEs from data, in which the time derivative term is euler-discretized and the constrained convolution kernel approximates the differential operator. The method proposed in the work of Wang, Liu and Wang (2022) can reconstruct the overall velocity field and pressure field with high resolution from sparse velocity information. By adding a convection diffusion equation to N-S equations, the flow field can be restored from the concentration of the carrier in the fluid (Raissi, Yazdani and Karniadakis, 2020).

Although data-driven solutions have been widely used, they have certain limitations. Methods that reduce label data and rely more on known equations are widely concerned. Therefore, there is growing interest in methods that reduce the need for labeled data and rely more on known equations. One such method is the PINN proposed by Raissi, Perdikaris and Karniadakis (2017a,b). PINN constructs the residuals using the control equations of PDEs and the identity of the boundary conditions. The sum of the residuals is then used to construct the loss function. To further improve the

performance of PINN, several modifications have been proposed. For example, Kani and Elsheikh (2018) combined PINN with orthogonal decomposition (POD) and discrete empirical interpolation method (DEIM) to provide a high-precision reduced order model of nonlinear dynamic systems and reduce the computational complexity of high-fidelity numerical simulations. Additionally, Jagtap, Kawaguchi and Karniadakis (2020) proposed the adaptive swish function to enhance the efficiency, robustness, and accuracy of PINN in approaching nonlinear functions and PDEs. Ranade, Hill and Pathak (2021) implemented a finite-volume based numerical schemes inside the computational graph, which is based on CNN. Dwivedi and Srinivasan (2020) proposed a distributed version of PINN, where the learning problem is decomposed into smaller regions of the computational domain and a physical compatibility condition is enforced in between neighboring domains. Bandai and Ghezzehei (2021) used the PINN framework composed of three DNNs to inverse the parameters of Richardson Richards equations, and achieved better results than one DNN. The multi-scale deep neural network (MscaleDNN) method was proposed to accelerate the convergence of high frequency (Wang, Zhang and Cai, 2020; Liu, Cai and Xu, 2020), the core idea is to stretch the objective function at different scales in the radial direction.

PINN has been proved to be able to solve multiple specification PDEs, and can handle multiple applications involving physics, chemistry and biology (Amini Niaki, Haghighat, Campbell, Poursartip and Vaziri, 2021; Wang, Wang and Perdikaris, 2021; Yang, Meng and Karniadakis, 2021; Liu and Wang, 2019; Snaiki, 2019; Zhao and Zhang, 2020). PINN also has atypical applications. Schiassi, D'Ambrosio, Drozd, Curti and Furfaro (2022) proposed a new framework for trajectory transfer optimization control, which obtains the first-order necessary conditions for the optimal control problem by applying the Pontryagin minimum principle. At this point, PINN transform solving partial differential problems into optimal control problems. So for logistics and transportation problems (Dulebenets, 2021; Kavoosi, Dulebenets, Abioye, Pasha, Theophilus, Wang, Kampmann and Mikijeljević, 2019a; Pasha, Nwodu, Fathollahi-Fard, Tian, Li, Wang and Dulebenets, 2022; Kavoosi, Dulebenets, Abioye, Pasha, Wang and Chi, 2019b; Rabbani, Oladzad-Abbasabady and Akbarian-Saravi, 2022), the same solution approach can also be used. The model (Barreau, Aguiar, Liu and Johansson, 2021) used assumes noisy measurements and a partially unknown first-order model to solve the problem of traffic density reconstruction using measurements from probe vehicles (PVs) with a low penetration rate. Using PINN framework to solve complex PDEs, such as N-S equations, is the focus of our work. Mao, Jagtap and Karniadakis (2020) investigated the possibility of using PINN to approximate the Euler equations that model high-speed aerodynamic flows. Mao et al. (2020) proposed Physics Informed Extreme Learning Machine (PIELM), which is a rapid version and demonstrated to solve N-S equations in a lid-driven cavity at low Reynolds numbers. Ranade et al. (2021) proposed the DiscretizationNet, which employs a generative CNN-based encoder–decoder model with PDE variables as both input and output features. DiscretizationNet is demonstrated to solve the steady, incompressible N-S equations in 3-D for several cases such as, lid-driven cavity, flow past a cylinder and conjugate heat transfer.

The above mentioned method mainly optimizes PINN by modifying the network structure. Another type of method mainly focuses on processing the equations itself to adapt to th neural networks. By useing arbitrarily accurate implicit Runge–Kutta time stepping schemes with unlimited number of stages, Raissi, Perdikaris and Karniadakis (2019) proposed discrete time models. Lyu, Zhang, Chen and Chen (2022) decomposed the order of differentiation to reduce complexity and avoid seeking high-order derivatives for a single neural network. Theory-guided hard constraint projection (HCP) (Chen, Huang, Zhang, Zeng, Wang, Zhang and Yan, 2021) used finite difference format templates to construct projection operators, and uses the objective function values obtained after projection as the target learning of the neural network. Yang et al. (2021) proposed the PhysGeoNet to solve the N-S equations using the finite difference discretizations of PDEs residuals in the neural network loss formulation.

The core idea of this paper is to assume that the current outputs of PINN are correct, and then investigate what the future and past flow fields should be. For this reason, we introduce CBS algorithm, which is widely used in the finite element method, into PINN. In the following examples, we only use the initial and boundary conditions to solve the equations without any labeled data. There are two main types of N-S equations: compressible and incompressible. The primary difference between compressible and incompressible flows is the variation of density with pressure and temperature, which leads to different equations for their motion. This method can solve the special form of compressible N-S equations——Shallow-Water equations, and incompressible N-S equations. Compared with the traditional PINN, this method does not consider the weights of output variables, and the calculation cost is smaller. There are 23 buoys and 32 sonar buoys that can be publicly accessed within China. The accumulated oceanographic hydrological data has exceeded 50 million records since 2014. These data exhibit sparse spatial coverage but dense temporal resolution. Traditional spatial discretization methods cannot effectively utilize these data. Processing such data is what our method

excels at. We show the progress of a solitary wave onto a shelving beach and the dispersion of the hot water in the flow to explain the advantages of ocean flow field estimation. By solving incompressible equations with exact solutions, we prove this method's correctness and universality.

2. PINN based on CBS

During the process of data fitting, neural networks often learn low frequencies before gradually learning high frequencies. This phenomenon is referred to as the Frequency Principle (F-Principle) (Xu, Zhang and Xiao, 2019; Xu, Zhang, Luo, Xiao and Ma, 2020). Gradient descent naturally aims to eliminate low-frequency errors, while high-dimensional errors cannot be eliminated. In fact, the F-Principle is also evident in the finite element method of N-S equations, such as the limitation of time step and grid density (Codina, Vázquez and Zienkiewicz, 1998). The F-Principle reveals that high frequency disasters can occur in neural networks, and the training and generalization difficulties caused by these disasters cannot be easily alleviated through simple parameter adjustments.

The MscaleDNN method can accelerate the convergence of high frequencies. The original MscaleDNN has two similar, but different, network structures, as shown in Figure 1. Both network structures are superior to fully connected networks. However, MscaleDNN-2, which appears to have a simpler structure, exhibits better performance than MscaleDNN-1. Before discussing why MscaleDNN-2 outperforms MscaleDNN-1, it is important to consider the following question: is it necessary to share parameters among output variables?
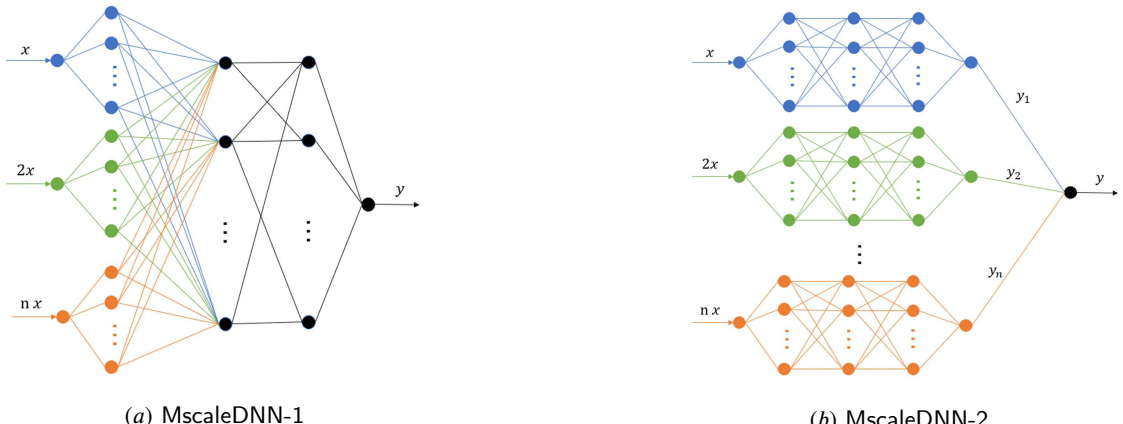

(*a*) MscaleDNN-1   (*b*) MscaleDNN-2

Figure 1: Two different network structures of MscaleDNN. The input set is a set of $\mathbf{x} = (x, 2x, ..., nx)$, and the output is y.

Suppose there exists a special solution of the N-S equations, where the velocity u_1 in the x direction varies with time, while the velocity u_2 in the y direction is constant. When u_1 and u_2 are fully connected, u_2 is not affected by time, so the weights coefficient of time in the full connection layer will be reduced. Meanwhile, u_1 is time-varying, and the weights reduction of time will cause the residuals related to u_1 to fail to converge, and vice versa. In fact, if we observe the partial derivative of the output u_1 and u_2 with respect to time under full connection, we will find that the two always remain at the same order of magnitude. This leads to the fact that the full connection between output parameters cannot converge in the case mentioned above, which also explains why MscaleDNN-2 is better than MscaleDNN-1. To some extent, MscaleDNN-2 achieves the separation of output parameters.

It is important to recognize that neural networks and the finite element method belong to the time-space approximation method. The finite element method, without specific algorithms, cannot solve complex problems, and similarly, the neural network also requires specific algorithms to achieve desirable results. After separating the output variables, we naturally consider an algorithm commonly used in the finite element method - CBS.

2.1. Characteristic-based split algorithm

The basic form of the N-S equations is as follows, and the shallow-water equations and incompressible-flow equations, which are mentioned later, are variant forms of it.

Conservation of mass:

$$\frac{\partial \rho}{\partial t} = \frac{1}{c^2}\frac{\partial p}{\partial t} = -\frac{\partial U_i}{\partial x_i} \tag{1}$$

Conservation of momentum:

$$\frac{\partial U_i}{\partial t} = -\frac{\partial}{\partial x_j}\left(u_j U_i\right) + \frac{\partial \tau_{ij}}{\partial x_j} - \frac{\partial p}{\partial x_i} - Q_i \tag{2}$$

where $i = direction$, $U_i = \rho u_i$, ρ is the density, p is the pressure, c is the speed of sound, u_i is the velocity component in the i direction, and T is the absolute temperature. Q is body forces, and Q_i is the component of Q in the i direction and the corrdinate axes are referred to as x_i. τ_{ij} is the deflection stress component, satisfying

$$\tau_{ij} = \mu\left(\frac{\partial U_i}{\partial x_j} + \frac{\partial U_j}{\partial x_i} - \frac{2}{3}\delta_{ij}\frac{\partial U_k}{\partial x_k}\right) \tag{3}$$

where δ_{ij} is Kronecker delta. If $i = j$, $\delta_{ij} = 1$; otherwise $\delta_{ij} = 0$. μ is the viscosity coefficient.

For the convenience of calculation, we use the nondimensional form of each variable:

$$t = \frac{\bar{t}u_\infty}{L}, x_i = \frac{\bar{x}_i}{L}, \rho = \frac{\rho}{\rho_\infty}, p = \frac{\bar{p}}{\rho_\infty u_\infty^2}$$

$$u_i = \frac{\bar{u}_i}{u_\infty}, \mathrm{Re} = \frac{u_\infty L}{v_\infty}, g_i = \frac{\bar{g}_i}{u_\infty^2}, v = \frac{\bar{v}}{v_\infty}$$

In the finite element calculation, we discretize the equation in the time direction Codina et al. (1998). Then Eq. (2) can be inferred as follows.

$$\frac{U_i^{n+1} - U_i^n}{\Delta t} = -\frac{\partial}{\partial x_j}\left(u_j U_i\right)^n + \frac{\partial \tau_{ij}^n}{\partial x_j} - \frac{\partial p^{n+\theta}}{\partial x_i} + Q_i^n + \left(\frac{\Delta t}{2}u_k\frac{\partial}{\partial x_k}\left(\frac{\partial}{\partial x_j}\left(u_j U_i\right) - \frac{\partial p}{\partial x_i} + Q_i\right)\right)^n \tag{4}$$

where $p^{n+\theta}$ represents the pressure value at time $t = t^n + \theta\Delta t$. Δt represents the time step and $\theta \in (0, 1)$. It further follows that

$$\frac{\partial p^{n+\theta}}{\partial x_i} = \theta\frac{\partial p^{n+1}}{\partial x_i} + (1-\theta)\frac{\partial p^n}{\partial x_i}$$

$$\frac{\partial p^{n-\theta}}{\partial x_i} = \theta\frac{\partial p^{n-1}}{\partial x_i} + (1-\theta)\frac{\partial p^n}{\partial x_i} \tag{5}$$

At this stage, we utilize the CBS algorithm Zienkiewicz, Taylor and Nithiarasu (2014) to substitute a suitable approximation, allowing for the calculation to be performed before obtaining p^{n+1}.

By introducing the auxiliary variables ΔU_i^* and ΔU_i^{**}, we can split Eq. (4) into two parts

$$\frac{U_i^{n+1} - U_i^n}{\Delta t} = \frac{\Delta U_i^*}{\Delta t} + \frac{\Delta U_i^{**}}{\Delta t} \tag{6}$$

$$\frac{\Delta U_i^*}{\Delta t} = -\frac{\partial}{\partial x_j}\left(u_j U_i\right)^n + \frac{\partial \tau_{ij}^n}{\partial x_j} + Q_i^n + \left(\frac{\Delta t}{2}u_k\frac{\partial}{\partial x_k}\left(\frac{\partial}{\partial x_j}\left(u_j U_i\right) + Q_i\right)\right)^n \tag{7}$$

$$\frac{\Delta U_i^{**}}{\Delta t} = -\frac{\partial p^{n+\theta_2}}{\partial x_i} + \frac{\Delta t}{2}u_k\frac{\partial^2 p^n}{\partial x_k\partial x_i} \tag{8}$$

Eq. (7) is solved by an explicit time step applied to the discretized form. Eq. (8) is obtained once $\Delta p = p^{n+1} - p^n$ is evaluated. From Eq. (1), we have

$$\frac{\Delta \rho}{\Delta t} = \frac{1}{c^2} \frac{\Delta p}{\Delta t} = -\frac{\partial U_i^{n+\theta_1}}{\partial x_i} = -\left[\frac{\partial U_i^n}{\partial x_i} + \theta_1 \frac{\partial \Delta U_i}{\partial x_i}\right] \tag{9}$$

Replacing ΔU_i by ΔU_i^* , using Eq. (6) and Eq. (8) and rearranging and neglecting third- and higher-order terms, we obtain

$$\frac{\Delta \rho}{\Delta t} = \frac{1}{c^2} \frac{\Delta p}{\Delta t} = -\frac{\partial U_i^n}{\partial x_i} - \theta_1 \frac{\partial \Delta U_i^*}{\partial x_i} + \Delta t \theta_1 \frac{\partial^2 p^{n+\theta_2}}{\partial x_i \partial x_i} \tag{10}$$

In the equations above, $0.5 \leq \theta_1 \leq 1.0$ and $\theta_2 = 0$ for explicit scheme, while $0.5 \leq \theta_1 \leq 1.0$ and $0.5 \leq \theta_2 \leq 1.0$ for the semi-implicit scheme. In the following calculation process, we chose the semi-implicit scheme with $\theta_1 = \theta_2 = 0.5$. The governing equations can be solved after spatial discretization in the following order:

- Step 1: use Eq. (7) to obtain ΔU_i^*.

- Step 2: use Eq. (10) to obtain Δp.

- Step 3: use Eq. (8) to obtain ΔU_i^{**} thus establishing the values of U_i and p.

After completing the calculation to establish ΔU_i and Δp, the transport equation is handled independently, as discussed in Section 3.3.

The CBS algorithm was initially used in the finite element method, and it retains second-order accuracy in the calculation process. While it is not impossible to achieve higher-order accuracy using neural networks, the amount of calculation required increases exponentially. Second-order accuracy has been demonstrated to be accurate enough in the finite difference method Shankar and Deshpande (2000); therefore, no higher-order CBS algorithm is derived in this study.

2.2. Physics-informed neural network combined with characteristic-based split method

A PINN is essentially a DNN that can be used to approximate the solution determined by the data and PDEs. A residual neural network can be expressed as

$$(\mathbf{u}, p) = F_{NN}(\mathbf{x}, t; \Theta) \tag{11}$$

where F_{NN} represents the neural network, whose inputs are space coordinates $\mathbf{x} = (x_1, x_2, x_3)$ and time t. The parameter Θ represents the trainable variables. The outputs of the neural network are velocity vector $\mathbf{u} = (u_1, u_2, u_3)$ and pressure p. We set up separate networks for each output and use independent optimizer and learning rate for each network. In the process of selecting sampling points, we think the sampling points should meet certain requirements. In the finite element method, there must be at least ten points in a wavelength to correctly describe the waveform without divergence. Random sampling does not necessarily ensure that convergence requirements are satisfied everywhere in the space. If the random sampling result causes divergence, it will be better to fix the sampling points. The examples selected in the following sections are all in two-dimensional rectangular space, so the sampling points are selected as the structured grid. In fact, the unstructured mesh in the finite element method can also be selected as the sampling points. The time interval Δt is fixed. The calculation steps are as follows:

Step 1,

Use input N sampling points $(\mathbf{x}, t)^j$ to obtain the initial output $(\mathbf{u}, p)_b^j$. ΔU_i^* can be calculated by Eq. (7). We consider $(\mathbf{u}, t)_b^j$ as prior information, similar to boundary conditions, initial state and label data. Thus, we combine $(\mathbf{u}, t)_b^j$, boundary conditions, initial state and label data together to construct prior information $(\mathbf{u}, p)_0^j$. The construction method involves replacing the original output point with the boundary conditions, initial state, and label data.

Step 2,

Use input N sampling points $(\mathbf{x}, t + \Delta t)^j$ to obtain p_a^j. Δp_a^j can be calculated by Eq. (10). To make the network satisfy the governing equations, the loss function in the p's network is defined as follows:
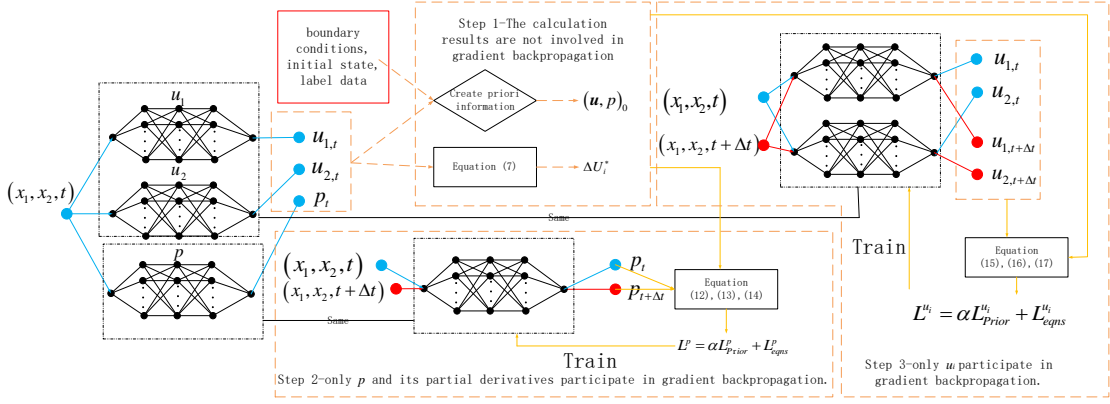
Figure 2: The solution process of PINN combined with CBS for solving N-S equations. The inputs are space coordinates $\mathbf{x} = (x_1, x_2, x_3)$ and time t, and the outputs are velocity vector $\mathbf{u} = (u_1, u_2, u_3)$ and pressure p. The physical laws are represented by N–S equations and automatic differentiation operators are used to obtain partial derivatives.

$$L^p = \alpha^p L^p_{Prior} + L^p_{eqns} \tag{12}$$

where α^p is a weighting coefficient. L^p_{Prior} and L^p_{eqns} are computed as

$$L^p_{Prior} = \sum_{j=1}^{N} \left(p_0^j - p_b^j \right)^2 / \Delta t^2 \tag{13}$$

$$L^p_{eqns} = \sum_{j=1}^{N} \left(p_a^j - p_0^j - \Delta p_a^j \right)^2 / \Delta t^2 \tag{14}$$

where L^p_{Prior} represents the loss between the prior information and the predicted data and L^p_{eqns} denotes the total residual of the N-S equations. Note that we use p_0 instead of p_b as the target result. This is also a common practice in the finite element method. Boundary conditions or known conditions replace the original data in the calculation process rather than after the calculation, which can obtain higher accuracy. Note that only p_a and its partial derivatives participate in gradient backpropagation.

Repeat Step 2 for K^p times and recalculate Δp_a^j.

Step 3,

Use input N sampling points $(\mathbf{x}, t + \Delta t)^j$ to obtain $u_{i,a}^j$. $\Delta U_{i,a}^j$ can be calculated by Eq. (8). ρ_0 and ρ_a can be calculated by Eq. (10). The loss function in the u_i's network is defined as follows:

$$L^{u_i} = \alpha^{u_i} L^{u_i}_{Prior} + L^{u_i}_{eqns} \tag{15}$$

where α^{u_i} is a weighting coefficient, and L^p_{Prior} and L^p_{eqns} are computed as

$$L^{u_i}_{Prior} = \sum_{j=1}^{N} \left(u_{i,0}^{\ j} - u_{i,b}^{\ j} \right)^2 / \Delta t^2 \tag{16}$$

$$L^{u_i}_{eqns} = \sum_{j=1}^{N} \left(u_{i,a}^{\ j} - \left(\rho_0 u_{i,0}^{\ j} + \Delta U_{i,a}^{\ j} \right) / \rho_a \right)^2 / \Delta t^2 \tag{17}$$

where $L_{Prior}^{u_i}$ represents the loss between the prior information and the predicted data, and $L_{eqns}^{u_i}$ denotes the total residual of the N-S equations. Note that only $u_{i,a}$ participate in gradient backpropagation.

Repeat Step 3 for K^{u_i} times and retain $\Delta U_{i,a}^j$.

Repeat Step 1-3 until L convergences to required accuracy, shown in Fig. 2. It can be seen that each input point in each step has two reference data: one is the prior information I_0, and the other is the posterior information I_1 obtained from Eq. (1)-(2). Therefore, theoretically, the final output result of each step will converge to $I_{final} = (I_1 + \alpha I_0)/(1 + \alpha)$. And the final loss L_{final} is related to the initial loss L_{init} as $L_{final} >= \frac{\alpha}{(1+\alpha)} L_{init}$. Hence, when loss decreases by $\frac{1}{2(1+\alpha)} L_{init}$, there is no need to increase K. When α decreases, the convergence speed will accelerate, but it is more likely to diverge.If the output continues to diverge, we should increase the corresponding α. Initially, α should be set to a larger value to prevent divergence, and then adjusted to a smaller value after stabilizing to speed up convergence. As α may change during the training process, the values of α mentioned below will represent the last set values.

It should be noted that the theoretical convergence result of this method does not depend on the network structure. When the network can fit the results with the required accuracy, changing the network structure will only affect the convergence rate. Therefore, all the networks mentioned below have the same network structure: the number of hidden layers $N_{layer} = 6$, the number of neurons $N_{cell} = 128$ in each hidden layer, and the activation function is the Swish function $\sigma(x) = \frac{x}{1+e^{-x}}$. To compute the residuals of the N-S equations, the partial differential operators are calculated using automatic differentiation (AD), which can be directly formulated in the deep learning framework, such as using "torch.autograd.grad" in Torch. In AD, the derivatives in the governing equations are approximated by the derivatives of the output with respect to the input of the PINNs. The use of "with torch.no_ Grad()" indicates that the current calculation does not require backpropagation.

The following is divided into two parts: 1. Use the shallow-water equations to solve the solitary wave problem, and it is pointed out that the separation of output parameters is more suitable for practical engineering applications; and 2. Solve the incompressible N-S equations with exact solutions and prove the method's correctness and universality.

2.3. Autograd mechanics and backpropagation

Our work is conducted within the framework of PyTorch, and we will briefly introduce its autograd mechanics and backpropagation mechanism, which complement each other. PyTorch is an open-source machine learning library that is primarily used for developing deep learning models. PyTorch provides a dynamic computational graph, which allows for easy debugging and flexibility in model design. The following analysis is based on the official PyTorch documentation, available at https://pytorch.org/docs/2.0/notes/autograd.html#autograd-mechanics.

Each variable in PyTorch has a *creator* attribute that points to the function that takes it as output. This is the entry point of a directed acyclic graph (DAG) composed of Function objects as nodes. The reference between them represents the edge of the graph. Every time an operation is executed, a new function representing it is instantiated, its $forward()$ method is called, and the *creator* of the variable it outputs is set to this function. By tracking the path from any variable to the leaf node, the sequence of operations used to generate the data can be reconstructed, and the gradient can be automatically calculated.
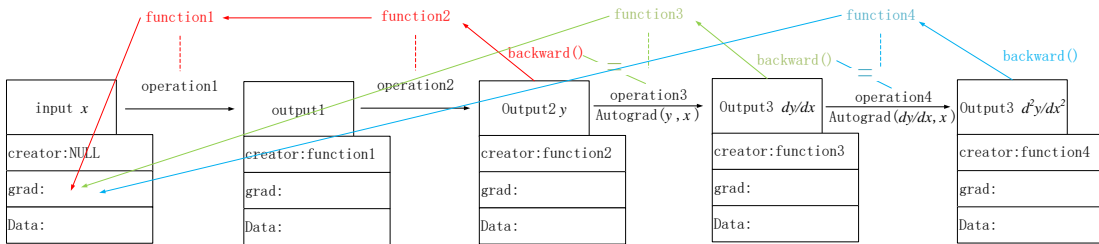

Figure 3: The brief process of autograd mechanics.

As depicted in Fig. 3, let us assume that we have an input variable x (with a data type of Variable) that is provided by the user, and thus its *creator* is NULL. After the first data operation, operation1 (such as addition, subtraction, multiplication, and division), the output1 variable (with a data type of Variable) is generated. In this process, a new instance of function1 (with a data type of Function) is automatically created, and the *creator* of output1 is set to this

Table 1
The memory occupation increment as the order of differentiation increases under autograd mechanics. The neural network architecture is 9 layers and 20 neurons per layer. The training data is $N = 20000$.

Derivative order	dy/dx	d^2y/dx^2	d^3y/dx^3	d^4y/dx^4
memory(Mb)	48	120	280	640

function1. Subsequently, output1 undergoes another data operation to generate output2, which also generates another instance of function2. The *creator* of output2 y is function2.

During the forward propagation process, function1 and function2 record the operation history of the input x. When y runs $backward()$, it causes function2 and function1 to automatically calculate the derivative value of x in reverse and store it in the $grad$ attribute. At the same time, the graph is destroyed, and memory is reclaimed. When using $Autograd(y, x)$ to calculate dy/dx, it is equivalent to using $backward()$ without destroying the graph and generating a new function3. Due to the involvement of function2, function1 and their derivatives in function3, function3 occupies much more memory than the sum of function2 and function1. Moreover, its $backward()$ consumes more computing power. Similarly, when using $Autograd(dy/dx, x)$ to calculate d^2y/dx^2, function4 is generated and occupies more memory than function3. For instance, if a single-input single-output network has a network structure of 9 layers and 20 neurons per layer, and the training data is $N = 20000$, the memory occupation increment as the order of differentiation increases is shown in Table 1.

As we can see, the memory occupation and the computing power required for backpropagation both increase exponentially as the order of differentiation increases. Therefore, by blocking the backpropagation of higher-order partial derivatives, we can significantly reduce the consumption of memory and computing power by destroying the corresponding function and preventing backward calculation.

3. Shallow Water Problems

The shallow-water equations are a set of partial differential equations that describe the behavior of fluids with a small depth compared to their horizontal extent. They are widely used to model the motion of fluids in oceans, lakes, and other bodies of water, as well as the flow of air in the atmosphere. The isothermal compressible folw equations can be transformed into the depth integrated shallow-water equations with the variables being changed as follows:

$$\rho\,(density) \rightarrow h\,(depth)$$
$$u_i\,(velocity) \rightarrow \bar{u}_i\,(mean-velocity)$$
$$p\,(pressure) \rightarrow \frac{1}{2}g\left(h^2 - H^2\right)$$

It can be written in a convenient form for the general CBS formulation as

$$\frac{\partial h}{\partial t} + \frac{\partial U_i}{\partial x_i} = 0 \tag{18}$$

$$\frac{\partial U_i}{\partial t} + \frac{\partial \left(\bar{u}_j U_i\right)}{\partial x_j} + \frac{\partial}{\partial x_i}\left(\frac{1}{2}g\left(h^2 - H^2\right)\right) + Q_i = 0 \tag{19}$$

where $U_i = h\bar{u}_i$, and H is the mean-depth. The rest of the variables are the same as those described before. Set $Q_i = 0$. The three essential steps of the CBS scheme can be written in its semi-discrete form as

Step 1,

$$\Delta U_{i,a}^* = \Delta t\left[-\frac{\partial\left(\bar{u}_j U_i\right)}{\partial x_j} + \frac{\Delta t}{2}u_k\frac{\partial}{\partial x_i}\left(\frac{\partial\left(\bar{u}_j U_i\right)}{\partial x_j}\right)\right]^n \tag{20}$$

Step 2,

$$\Delta h_a = -\Delta t\left[\frac{\partial\left(U_i^n\right)}{\partial x_j} + \theta_1\frac{\partial\Delta U_i^*}{\partial x_i} - \Delta t\theta_1\frac{\partial^2 p^{n+\theta_2}}{\partial x_i\partial x_i}\right] \tag{21}$$

$$L^h_{Prior} = \sum_{j=1}^{N} \left(h_0 - h_b \right)^2 / \Delta t^2 \tag{22}$$

$$L^h_{eqns} = \sum_{j=1}^{N} \left(h_a - h_0 - \Delta h_a \right)^2 / \Delta t^2 \tag{23}$$

Step 3,

$$\Delta U_{i,a} = \Delta U^*_{i,a} - \Delta t \frac{\partial p_i^{n+\theta_2}}{\partial x_i} + \frac{\Delta t^2}{2} \bar{u}_k \frac{\partial^2 p^n}{\partial x_k \partial x_i} \tag{24}$$

$$L^{u_i}_{Prior} = \sum_{j=1}^{N} \left(u_{i,0}{}^j - u_{i,b}{}^j \right)^2 / \Delta t^2 \tag{25}$$

$$L^{u_i}_{eqns} = \sum_{j=1}^{N} \left(u_{i,a}{}^j - \left(h_0 u_{i,0}{}^j + \Delta U_{i,a}{}^j \right) / h_a \right)^2 / \Delta t^2 \tag{26}$$

with $p = g(h^2 - H^2)$.

After Step 1, the calculation graph generated in this step will be destroyed and only the value of ΔU^*_i will be retained. This step does not involve backpropagation. After Step 2, only the calculation graphs that generate $\frac{\partial^2 p}{\partial x_i \partial x_i}$ and h are retained. After Step 3, only the calculation graph of u_i is retained. Only parameters related to the retained computational graph can participate in backpropagation.

Solitary waves, also known as solitons, are localized waves that maintain their shape and speed as they propagate through a medium. Unlike most waves, which disperse and lose energy as they travel, solitary waves can travel long distances without changing their shape or size. Solitary waves have many practical applications, including in optical communications, where they can be used to transmit information without distortion or attenuation, and in oceanography, where they can help to model and predict the behavior of ocean waves.

The propagation process of a solitary wave in a flat-bottomed flume has an accurate solution, which can be used to verify the correctness of the method. In this case, the wave height and velocity of solitary waves do not change during the propagation process in the flat-bottomed flume.

To make the problem more complex, we can compute the propagation process of solitary waves onto a shelving beach, as shown in Fig. 4. The propagation process of a solitary wave Löhner, Morgan and Zienkiewicz (1984) can be approximately expressed as:

$$\eta(x_1, x_2, t) = a \operatorname{sech}^2 \left(\sqrt{3a/4h^3} \times \left(x_1 - 30 - Ct \right) \right)$$
$$u_1(x_1, x_2, t) = -(l + 1/2a)\eta / \left((x_1 - Ct)/30 + \eta \right) \tag{27}$$

with $u_2(x, y, t) = 0$, $a = 0.1$, $\eta = h - H$ and $C = \sqrt{gh(1 + H/h)}$. Set $g = 1.0$, so $C \approx 1.0$. It should be pointed out that the above equation is its approximate expression. But regardless of whether the equation is correct or not, this method can always derive the solution that meets the priori information and shallow-water equations.

3.1. Solve when the initial state is known

The computation is carried out in the domain of $0 \le x_1 \le 40$, $0 \le x_2 \le 5$ and $0 \le t \le 10$. Sampling interval is $\Delta x_1 = 0.25$, $\Delta x_2 = 0.25$ and $\Delta t = 0.125$. So the total number of sampling points is $N = 161 * 21 * 81 = 273861$. All
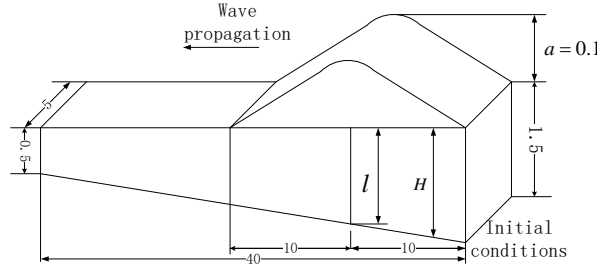
Figure 4: Solitary wave onto a shelving beach.

three networks use the Adam optimizer and $\alpha^p = \alpha^{u_1} = \alpha^{u_2} = 1$. The initial state equations and boundary conditions are

$$\eta(x_1, x_2, 0) = a\mathrm{sech}^2 \left(\sqrt{3a/4h^3} \times (x_1 - 30) \right)$$
$$u_1(x_1, x_2, 0) = -(l + 1/2a)\,\eta/\left(x_1/30 + \eta\right) \tag{28}$$

$$\begin{cases} u_1\left(0, x_2, t\right) = 0, u_1\left(40, x_2, t\right) = 0 \\ u_2\left(x_1, 0, t\right) = 0, u_2\left(x_1, 5, t\right) = 0 \end{cases} \tag{29}$$

The pseudo code of the calculation process is as follows:

Algorithm 1 shallow-water problem

1: Set $\Delta t = 0.125$
2: get $h_{ini}, \bar{u}_{i,ini}$ by Eq. (28)
3: **for** step in range(1000) **do**
4:     //Step 1
5:     input N points $(\mathbf{x}, t)$ to obtain $\bar{u}_{i,b}, h_b$
6:     with torch.no_grad():   ▷ Create priori information
7:         $h_0, \bar{u}_{i,0} = clone(\bar{u}_{i,b}, h_b)$
8:         $h_0(:, t = 0), \bar{u}_{i,0}(:, t = 0) = h_{ini}, \bar{u}_{i,ini}$
9:         $\bar{u}_{1,0}(x_2 = 0, :) = \bar{u}_{1,0}(x_2 = 40, :) = 0$
10:        $\bar{u}_{2,0}(x_1 = 0, :) = \bar{u}_{2,0}(x_1 = 5, :) = 0$
11:     get $\Delta U_{i,a}^*$ by Eq. (20).
12:     //Step 2
13:     with torch.no_grad():   ▷ Prepare for Δh_a
14:         get $\frac{\partial(U_i^n)}{\partial x_j}, \frac{\partial \Delta U_i^*}{\partial x_i}$ by AD
15:     **for** k in range(K_h) **do**
16:         input N points $(\mathbf{x}, t)$ and $(\mathbf{x}, t + \Delta t)$ to obtain h_b and h_a, Respectively
17:         get $\frac{\partial^2 p^{n+\theta_2}}{\partial x_i \partial x_i}$ ▷ Gradient is not mandatory
18:         get Δh_a by Eq. (21)
19:         get L^h by Eqs. (22),(23)
20:         $L^h.backward()$ and use Adam Optimizer
21:     **end for**
22:     //Step 3
23:     with torch.no_grad():
24:         input N points $(\mathbf{x}, t + \Delta t)$ to obtain h_a
25:         get $\frac{\partial p_{i,a}}{\partial x_i}$

26:         get $\Delta U_{i,a}$ by Eq. (24)

27:     **for** k in range(K_{u_i}) **do**

28:         input N points $(\mathbf{x}, t)$ and $(\mathbf{x}, t + \Delta t)$ to obtain $\bar{u}_{i,b}$ and $\bar{u}_{i,a}$, Respectively

29:         get L^{u_i} by Eqs. (25),(26)

30:         $L^{u_i}.backward()$ and use Adam Optimizer
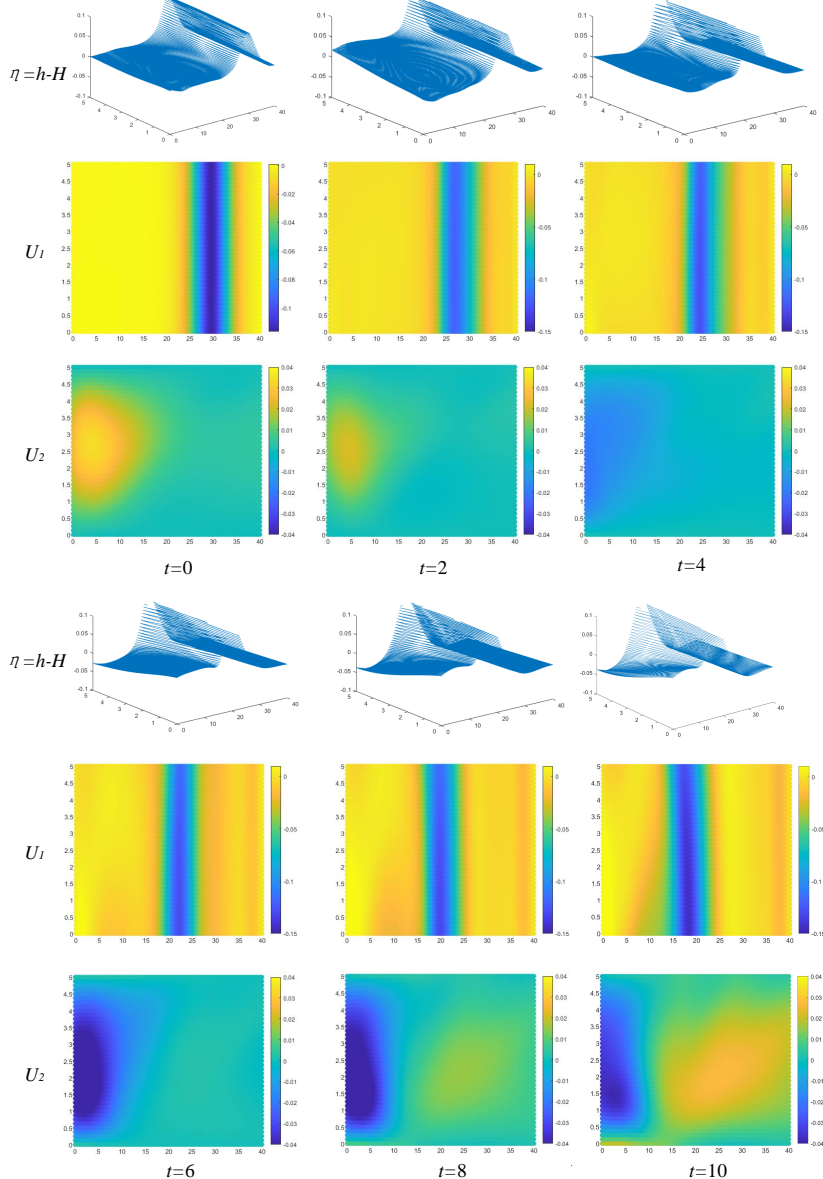
31:     **end for**

32: **end for**

Figure 5: Solitary wave in the inclined bottom flume. Results with incomplete initial conditions. From left to right are the numerical distributions of U_i and η in the computational domain at time $t = 0, 2, 4, 6, 8, 10$.

The initial state of u_2 is not provided in this case, so the conditions for solving the equations are incomplete. However, the neural network still gives a solution, as shown in Fig. 5. Initially, it was thought that when the conditions were incomplete, the result would tend to be a steady solution without a time term. However, it is evident that if the

Table 2

The position of the wave crest in the x_1-direction. The initial state is known with the initial state of u_2 is not provided.

t	0	2	4	6	8	10
position	30.0	27.3	24.8	22.5	20.5	18.0

calculation continues, u_2 will tend to diverge. Therefore, the neural network cannot provide a solution that goes beyond the conventional method and give the correct answer under insufficient conditions.

Although u_2 does not tend to 0 as expected, the solitary wave is still well-described by the neural network. The position of the wave crest in the x_1-direction over time is shown in Table 2. The propagation speed is approximately 1.2, which is not consistent with the expected value. However, the wave height increases during the propagation process, which is consistent with the theoretical results.

3.2. Solve when the intermediate state is known

In this section, we will discuss how to obtain the past and the future information when the intermediate time information is known. The boundary conditions are the same as those in Eq. (29). The intermediate state equations are

$$\eta(x_1, x_2, 5) = a\text{sech}^2\left(\sqrt{3a/4h^3} \times (x_1 - 25)\right)$$

$$u_1(x_1, x_2, 5) = -(l + 1/2a)\,\eta/\left((x_1 - 5)/30 + \eta\right) \tag{30}$$

$$u_2(x_1, x_2, 5) = 0$$

In the previous process, the networks only obtain the future flow field information from the current flow field. We make the networks obtain the past flow field information by adding the time-step items as follows:

Step 1,

Calculate $\Delta U_{i,a}^*$ and $\Delta U_{i,c}^*$ by Eq. (7) and Eq. (31).

$$\Delta U_{i,c}^* =$$
$$\Delta t\left[-\frac{\partial\left(\bar{u}_j U_i\right)}{\partial x_j} + \frac{\Delta t}{2}u_k\frac{\partial}{\partial x_i}\left(\frac{\partial\left(\bar{u}_j U_i\right)}{\partial x_j}\right)\right]^n \tag{31}$$

Step 2,

Use input $(\mathbf{x}, t - \Delta t)^j$ to obtain h_c^j. Change L_{eqns}^h as

$$L_{eqns}^h = \sum_{j=1}^{N}\left(h_a{}^j - h_0{}^j - \Delta h_a{}^j\right)^2/\Delta t^2 + \sum_{j=1}^{N}\left(h_c{}^j - h_0{}^j - \Delta h_c{}^j\right)^2/\Delta t^2 \tag{32}$$

Δh_c is computed as

$$\Delta h_c = \Delta t\left[\frac{\partial\left(U_i^n\right)}{\partial x_j} + \theta_1\frac{\partial \Delta U_i^*}{\partial x_i} - \Delta t\theta_1\frac{\partial^2 p^{n-\theta_2}}{\partial x_i\partial x_i}\right] \tag{33}$$

Step 3,

Use input $(\mathbf{x}, t - \Delta t)^j$ to obtain $u_{i,c}^j$. Change $L_{eqns}^{u_i}$ as

$$L_{eqns}^{u_i} = \sum_{j=1}^{N}\left(u_{i,a}{}^j - \left(h_0 u_{i,0}{}^j + \Delta U_{i,a}{}^j\right)/h_a\right)^2/\Delta t^2 + \sum_{j=1}^{N}\left(u_{i,c}{}^j - \left(h_0 u_{i,0}{}^j + \Delta U_{i,c}{}^j\right)/h_c\right)^2/\Delta t^2 \tag{34}$$

$\Delta U_{i,c}$ is computed as

$$\Delta U_{i,c} = \Delta U_{i,c}^* + \Delta t\frac{\partial p_i^{n-\theta_2}}{\partial x_i} + \frac{\Delta t^2}{2}\bar{u}_k\frac{\partial^2 p^n}{\partial x_k\partial x_i} \tag{35}$$
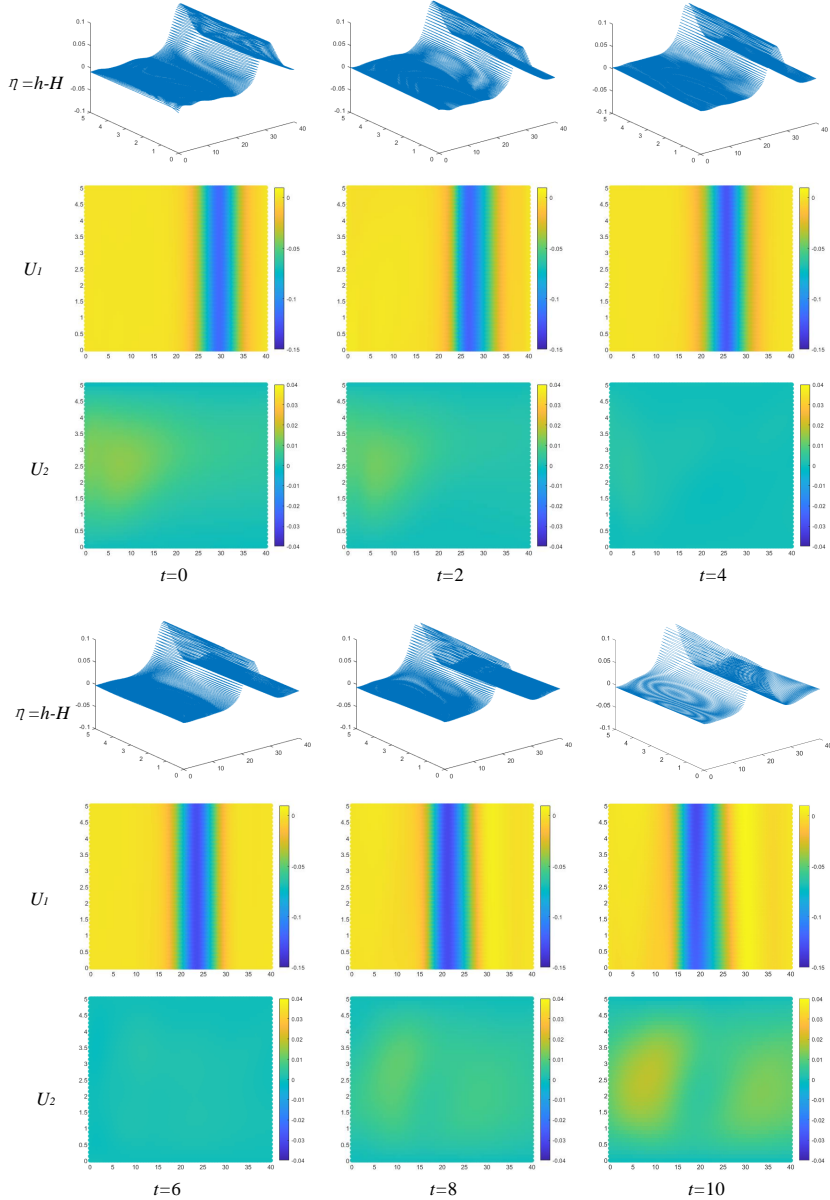
Figure 6: Solitary wave in the inclined bottom flume. Results with complete intermediate conditions. Results with incomplete initial conditions. From left to right are the numerical distributions of U_i and η in the computational domain at time $t = 0, 2, 4, 6, 8, 10$.

When other settings remain unchanged, the modifications mentioned above can achieve better results, as shown in Fig. 6. These modifications can improve the stability of the results, but they may also reduce the convergence speed. The position of the wave crest in the u_1-direction over time is shown in Table 3. The propagation speed is approximately 1.1, which is consistent with the expected value.

The finite element method inherently implies many boundary conditions, as parameters outside the calculation area do not exist mathematically, and their partial derivatives of all orders are zero. This has both advantages and disadvantages. On the one hand, it does not require setting boundary conditions for the parameter partial derivative term. However, it cannot deal with the reflection of waves at the boundary.

Table 3
The position of the wave crest in the x_1-direction. The intermediate state is known.

t	0	2	4	6	8	10
position	30.0	27.8	25.5	23.5	21.2	19.1

In contrast, the parameters of the neural network outside the calculation area still exist. Therefore, when the wave flows out of the calculation area, it will not be reflected. However, in some cases, more boundary conditions are needed. To address this, the time-step-back items are added in the above method. By considering both the time-step-back and time-step items simultaneously, the method partially achieves the effect that the partial derivatives of the boundary parameters are zero and can replace some boundary conditions.

3.3. Shallow-water transport

In engineering applications, it is often unnecessary to obtain all the information to guide production. It can be cost-effective to acquire only a part of the information. The separation of output parameters can solve this problem and make it more convenient for further calculations.

Shallow-water transport problems refer to the study of the transport of fluids with small depths compared to their horizontal extent, such as water in rivers, estuaries, and coastal regions. The transport of such fluids is governed by the shallow-water equations, which are a set of partial differential equations that describe the behavior of such fluids.

Shallow-water transport problems are important in many practical applications, including the management of water resources, flood prediction and control, and the design of hydraulic structures such as dams and levees. In these applications, it is essential to accurately predict the transport of water and other materials such as sediment and pollutants through the shallow-water system.

We can use the flow field information obtained above to calculate the dispersion of some quantities in the shallow-water. The depth-averaged transport equation can be calculated, in which the averaged velocities u have been determined independently. A typical shallow-water transport equation can be written as:

$$\frac{\partial (hT)}{\partial t} + \frac{\partial (h\bar{u}_i T)}{\partial x_i} - \frac{\partial}{\partial x_i}\left(hk\frac{\partial T}{\partial x_i}\right) + R = 0 \tag{36}$$

where h and $\bar{u}_i$ are the previously defined and computed quantities, k is an appropriate diffusion coefficient, and R is a source term. Set $R = 0$. The application of the CBS method for any scalar transport equation is straightforward, because of the absence of the pressure gradient term. Now a new time integration parameter θ_3 is introduced for the diffusion term such that $0 \leq \theta_3 \leq 1$. We used the method that considers both time-step and time-step-back items to reduce the boundary conditions. The form is:

$$\Delta hT_a = hT^{n+1} - hT^n = -\Delta t \left[\frac{\partial (h\bar{u}_i T_b)}{\partial x_i} - \frac{\Delta t}{2}u_k\frac{\partial}{\partial x_k}\left(\frac{\partial (h\bar{u}_i T_b)}{\partial x_i}\right)\right]^n + \Delta t\frac{\partial}{\partial x_i}\left(hk\frac{\partial T^{n+\theta_3}}{\partial x_i}\right) \tag{37}$$

$$\Delta hT_c = hT^{n-1} - hT^n = \Delta t \left[\frac{\partial (h\bar{u}_i T_b)}{\partial x_i} + \frac{\Delta t}{2}u_k\frac{\partial}{\partial x_k}\left(\frac{\partial (h\bar{u}_i T_b)}{\partial x_i}\right)\right]^n - \Delta t\frac{\partial}{\partial x_i}\left(hk\frac{\partial T^{n-\theta_3}}{\partial x_i}\right) \tag{38}$$

$$L^T_{eqns} = \sum_{j=1}^N \left(T_a^j - \left(h_0 T_0^j + \Delta hT_a{}^j\right)/h_a\right)^2/\Delta t^2 + \sum_{j=1}^N \left(T_c^j - \left(h_0 T_0^j + \Delta hT_c{}^j\right)/h_c\right)^2/\Delta t^2 \tag{39}$$

The computation is carried out in the domain of $20 \leq x_1 \leq 25$, $0 \leq x_2 \leq 5$ and $0 \leq t \leq 10$. The sampling intervals are $\Delta x_1 = 0.25$, $\Delta x_2 = 0.25$, and $\Delta t = 0.125$, resulting in a total number of sampling points of $N = 21 \times 21 \times 81 = 35,721$.

The network use the Adam optimizer with $\alpha^T = 10$. The initial state equation is

$$T(x, y, 0) = \frac{10}{\sqrt{2\pi}} \exp\left(-\left((x - 22.5)^2 + (y - 2.5)^2\right)/2\right) \tag{40}$$

The pseudo code of the calculation process is as follows:

Algorithm 2 shallow-water transport problem

1: Set $\Delta t = 0.125$
2: get T_{ini} by Eq. (40)
3: **for** step in range(1000) **do**
4:    input N points $(\mathbf{x}, t)$ to obtain $\bar{u}_i$, h and T_b
5:    with torch.no_grad():   ▷ Create priori information
6:       $T_0 = clone(T_b)$
7:       $T_0(:, t = 0) = T_{ini}$
8:    **for** k in range(K_T) **do**
9:       input N points $(\mathbf{x}, t)$, $(\mathbf{x}, t + \Delta t)$ and $(\mathbf{x}, t - \Delta t)$ to obtain T_b, T_a and T_c, Respectively
10:      with torch.no_grad():
11:         get $\Delta h T_a$ and $\Delta h T_c$ by Eqs. (37),(38)
12:      get L^T_{eqns} by Eqs. (39)
13:      $L^T.backward()$ and use Adam Optimizer
14:   **end for**
15: **end for**

Stable results can be obtained without boundary conditions, shown in Fig. 7. The temperature field shifts to the right due to the flow field, and the temperature decreases due to diffusion.
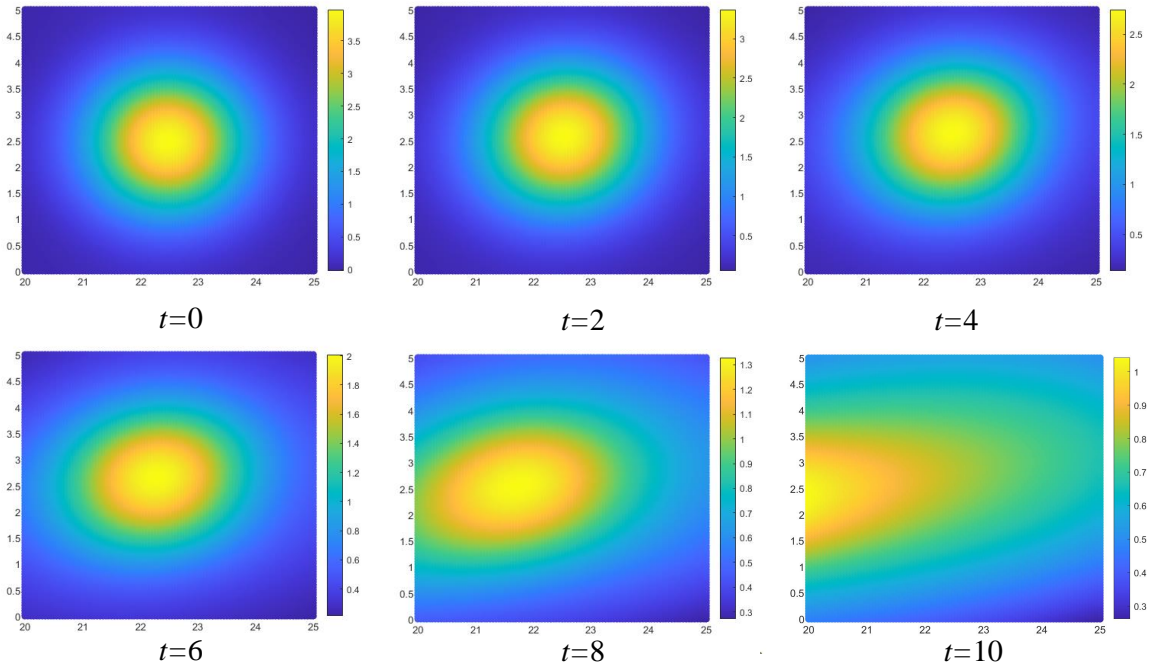

Figure 7: From left to right are temperature fields at time $t = 0, 2, 4, 6, 8, 10$.

4. Incompressible flow

Incompressible flow is a type of fluid flow in which the density of the fluid remains constant, or nearly constant, as it moves through a system. This means that the volume of the fluid is conserved as it flows, and the fluid is not compressed or expanded. Incompressible flow is a simplifying assumption that is often used in the study of fluid mechanics, as it allows for the use of simpler mathematical models and equations.

Incompressible flow has many practical applications, including in the design of pipes, pumps, and other fluid-handling equipment, as well as in the study of aerodynamics. In these applications, the assumption of incompressible flow allows for the use of simpler equations and models that can be used to predict the behavior of the fluid in the system.

As discussed in Section 3, the shallow water flow equation is a deformation of the N-S equations, and incompressible flow is a special case of the N-S equations. In the context of incompressible flow, we consider the limit as $c \to \infty$, and Eq. (1) becomes:

$$0 = -\frac{\partial u_i}{\partial x_i} \tag{41}$$

Momentum conservation

$$\frac{\partial u_i}{\partial t} = -\frac{\partial}{\partial x_j}\left(u_j u_i\right) + \frac{1}{\mathrm{Re}}\frac{\partial^2 u_i}{\partial x_j^2} - \frac{\partial p}{\partial x_i} \tag{42}$$

where Re represents the Reynolds number. The rest of the variables are the same as those described before. Obviously, such simplification leads to the pressure information loss. The change of p is affected by the current flow field. Water is generally considered as an incompressible flow, and its sound velocity is $c = 1480m/s$. In the finite element method, there are two ways to deal with it. One is to retain the p item in the mass formula, so the time accuracy will become extremely high. If the mesh size is $\Delta x = 0.1m$, then the time step should meet the requirement $\Delta t = 0.1/1480s$. The other is to use the implicit scheme like CBS. The three essential steps of the CBS scheme can be written in its semi-discrete form as

Step 1,

$$\Delta u_{i,a}^* = \Delta t \left[-\frac{\partial\left(u_j u_i\right)}{\partial x_j} + \frac{\Delta t}{2} u_k \frac{\partial}{\partial x_i}\left(\frac{\partial\left(u_j u_i\right)}{\partial x_j}\right) + \frac{1}{\mathrm{Re}}\frac{\partial^2 u_i}{\partial x_j^2} \right]^n \tag{43}$$

Step 2,

$$\Delta_a = \Delta t \left[\frac{\partial\left(u_i^n\right)}{\partial x_j} + \theta_1\frac{\partial\Delta u_{i,a}^*}{\partial x_i} + \Delta t\theta_1\frac{\partial^2 p^{n+\theta_2}}{\partial x_i\partial x_i} \right] \tag{44}$$

$$L_{Prior}^p = \sum_{j=1}^N \left(p_0^j - p_b^j\right)^2 / \Delta t^2 \tag{45}$$

$$L_{eqns}^p = \sum_{j=1}^N \left(\Delta_a\right)^2 / \Delta t^2 \tag{46}$$

Step 3,

$$\Delta u_{i,a} = \Delta u_{i,a}^* - \Delta t\frac{\partial p_i^{n+\theta_2}}{\partial x_i} + \frac{\Delta t^2}{2} u_k\frac{\partial^2 p^n}{\partial x_k\partial x_i} \tag{47}$$

$$L_{Prior}^{u_i} = \sum_{j=1}^N \left(u_{i,0}{}^j - u_{i,b}{}^j\right)^2 / \Delta t^2 \tag{48}$$

$$L_{eqns}^{u_i} = \sum_{j=1}^N \left(u_{i,a}^j - u_{i,0}^j - \Delta u_{i,a}{}^j\right)^2 / \Delta t^2 \tag{49}$$

After Step 1, the calculation graph generated in this step is destroyed and only the value of Δu_i^* is retained. This step does not involve backpropagation. After Step 2, only the calculation graphs that generate $\frac{\partial^2 p}{\partial x_i\partial x_i}$ and p are retained. After step 3, only the calculation graph of u_i is retained. Only parameters related to the retained computational graph can participate in backpropagation.
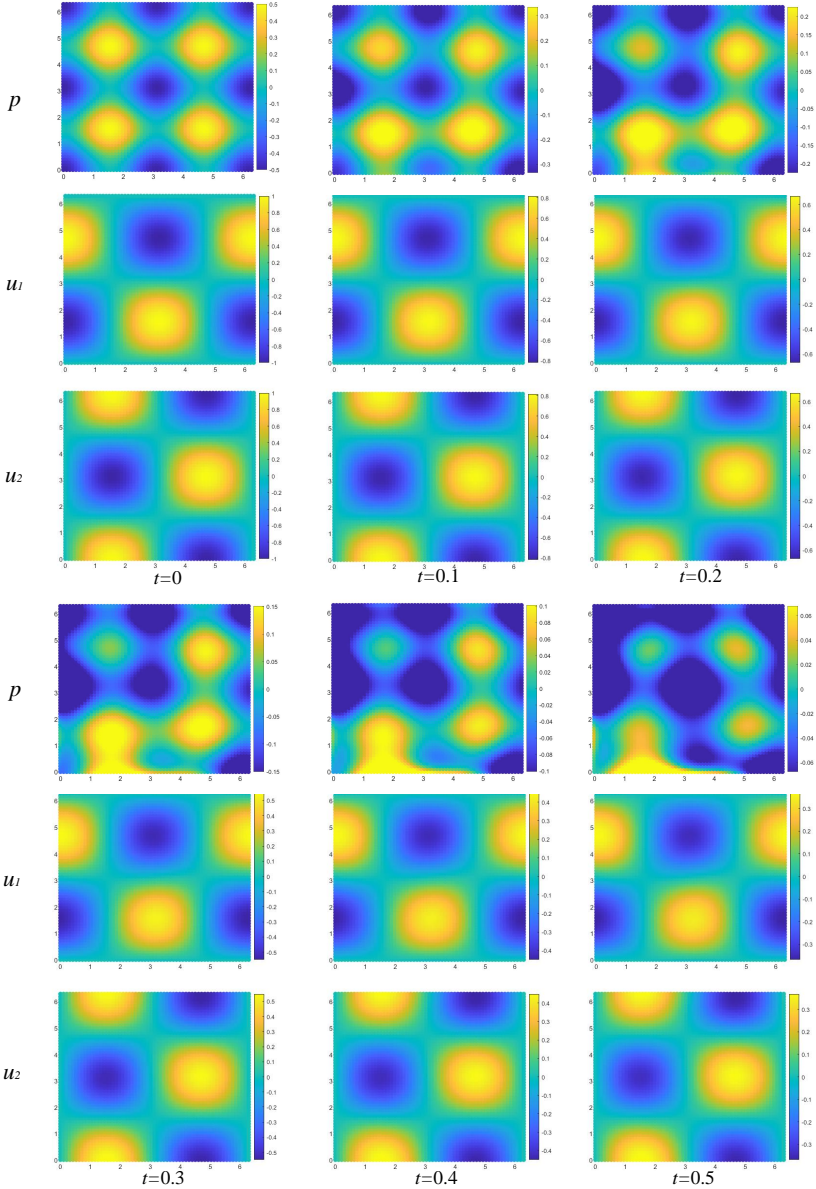
Figure 8: The spatial distribution of p, u_1 and u_2 from top to bottom. From left to right is their change with time. Boundary conditions without p.

4.1. Boundary conditions

We consider 2D Taylor's decaying vortices to check the method. When $Re = 1$, an exact 2D solution to Eqs. (41)-(42) given by F.R.S. (1923) and Ethier and Steinman (1994) is as follows:

$$
\begin{aligned}
u_1\left(x_1, x_2, t\right) &= -\cos\left(x_1\right)\sin\left(x_2\right)e^{-2t} \\
u_2\left(x_1, x_2, t\right) &= \sin\left(x_1\right)\cos\left(x_2\right)e^{-2t} \\
p\left(x_1, x_2, t\right) &= -0.25\left(\cos\left(2x_1\right) + \cos\left(2x_2\right)\right)e^{-4t}
\end{aligned} \tag{50}
$$

The computation is carried out in the domain of $0 \le x_1 \le 2\pi$, $0 \le x_2 \le 2\pi$ and $0 \le t \le 0.5$. The sampling intervals are $\Delta x_1 = 0.05\pi$, $\Delta x_2 = 0.05\pi$, and $\Delta t = 0.025$, resulting in a total number of sampling points of

$N = 41 \times 41 \times 21 = 35,301$. All three networks use the Adam optimizer and $\alpha^p = 0.01$, $\alpha^{u_1} = \alpha^{u_2} = 0.1$. The initial state equations and boundary conditions are

$$
\begin{aligned}
u_1\left(x_1, x_2, 0\right) &= -\cos\left(x_1\right)\sin\left(x_2\right) \\
u_2\left(x_1, x_2, 0\right) &= \sin\left(x_1\right)\cos\left(x_2\right) \\
p\left(x_1, x_2, 0\right) &= -0.25\left(\cos\left(2x_1\right) + \cos\left(2x_2\right)\right)
\end{aligned}
\tag{51}
$$

$$
\begin{cases}
u_1\left(0, x_2, t\right) = u_1\left(2\pi, x_2, t\right) = -\sin(x_2) \\
u_1\left(x_2, 0, t\right) = u_1\left(x_1, 2\pi, t\right) = 0 \\
u_2\left(0, x_2, t\right) = u_2\left(2\pi, x_2, t\right) = 0 \\
u_2\left(x_1, 0, t\right) = u_2\left(x_1, 2\pi, t\right) = \sin(x_1)
\end{cases}
\tag{52}
$$

The results are presented in Fig. 8. It can be observed that the results for u_1 and u_2 are more consistent with the exact solution, while p deviates significantly from the exact solution. It is evident that p exhibits significant leakage at the boundary.

In order to get the correct results, additional boundary conditions for pressure need to be added as

$$
\begin{cases}
p\left(0, x_2, t\right) = p\left(2\pi, x_2, t\right) = -0.25(1 + \cos(2x_2)) \\
p\left(x_1, 0, t\right) = p\left(x_1, 2\pi, t\right) = -0.25(1 + \cos(2x_1))
\end{cases}
\tag{53}
$$

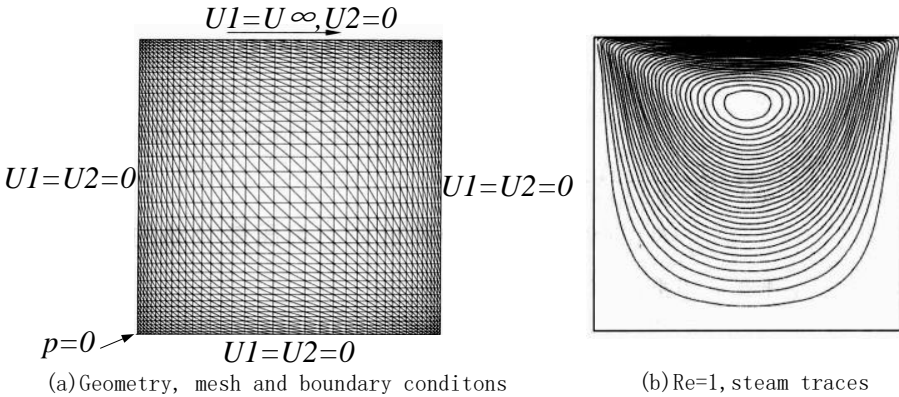(a) Geometry, mesh and boundary conditons

(b) Re=1, steam traces

Figure 9: Inconpressible flow in a lid-driven cavity. (a) Geometry, mesh and boundary conditions; (b) Re=1, steam traces.

A classic problem, namely a closed cavity driven by the motion of a lid (Shankar and Deshpande, 2000), highlights the need for additional boundary conditions, as illustrated in Fig. 9. The results demonstrate that the velocity component parallel to the wall has a significant impact on the overall flow field, emphasizing the role of the viscous term. In the finite element method, there are no parameters outside the computational domain, and the values on the boundaries are solely influenced by the parameters within the domain. However, in neural networks, parameters outside the computational domain can continuously affect the values on the boundaries. This is analogous to applying random parallel wall velocity components to the four walls of a cavity. Therefore, neural networks require more boundary conditions to constrain the results, whereas the finite element method can omit certain boundary conditions when dealing with some symmetric problems.

The pseudo code of the calculation process is as follows:

Algorithm 3 Incompressible N-S equations problem

1: Set $\Delta t = 0.005$
2: get $p_{ini}, u_{i,ini}$ by Eq. (28)
3: **for** step in range(1000) **do**
4:      //Step 1
5:      input N points $(\mathbf{x}, t)$ to obtain $\bar{u}_{i,b}, h_b$
6:      with torch.no_grad():   ▷ Create priori information
7:          $u_{i,0}, p_0 = clone(u_{i,b}, p_b)$
8:          $p_0(:, t = 0), u_{i,0}(:, t = 0) = p_{ini}, u_{i,ini}$
9:          add boundary conditions by Eqs. (52),(53)
10:     get $\Delta u_{i,a}^*$ by Eq. (43).
11:     //Step 2
12:     with torch.no_grad():   ▷ Prepare for Δp_a
13:         get $\frac{\partial (u_i^n)}{\partial x_j}, \frac{\partial \Delta u_i^*}{\partial x_i}$ by AD
14:     **for** k in range(K_p) **do**
15:         input N points $(\mathbf{x}, t)$ and $(\mathbf{x}, t + \Delta t)$ to obtain p_b and p_a, Respectively
16:         get $\frac{\partial^2 p^{n+\theta_2}}{\partial x_i \partial x_i}$ ▷ Gradient is mandatory
17:         get Δ_a by Eq. (44)
18:         get L^p by Eqs. (45),(46)
19:         $L^p.backward()$ and use Adam Optimizer
20:     **end for**
21:     //Step 3
22:     with torch.no_grad():
23:         input N points $(\mathbf{x}, t + \Delta t)$ to obtain p_a
24:         get $\frac{\partial p_{i,a}}{\partial x_i}$
25:         get $\Delta u_{i,a}$ by Eq. (47)
26:     **for** k in range(K_{u_i}) **do**
27:         input N points $(\mathbf{x}, t)$ and $(\mathbf{x}, t + \Delta t)$ to obtain $u_{i,b}$ and $u_{i,a}$, Respectively
28:         get L^{u_i} by Eqs. (48),(49)
29:         $L^{u_i}.backward()$ and use Adam Optimizer
30:     **end for**
31: **end for**

Set $\alpha^p = 0.01$, $\alpha^{u_1} = \alpha^{u_2} = 10$, while keeping all other conditions unchanged, the results obtained using Eq. (53) are presented in Fig. 10. The L_2 norm, which can be utilized to evaluate the accuracy of the results, is calculated for p, u_1, and u_2, resulting in values of 0.17, 0.017, and 0.015, respectively. Since p is a high-frequency parameter relative to u_1 and u_2, the F-principle is well reflected here. In this case, the simplest approach to address the issue is by reducing the time step Δt. By setting $\Delta t = 0.005$, while keeping all other conditions unchanged, the L_2 norm of p, u_1, and u_2 can be reduced to 0.13, 0.0069, and 0.0071, respectively, as shown in Fig. 11.

4.2. Factors that affect accuracy

Table 4 presents a detailed systematic study that quantifies the effect of different time-step sizes Δt. As shown in the table, it can be observed that decreasing the time-steps Δt leads to a reduction in the relative final prediction errors. By keeping $\Delta x_1 = 0.05\pi$, $\Delta x_2 = 0.05\pi$, and $\Delta t = 0.005$ constant, we vary the total calculation time t_{final} and present the resulting relative final prediction errors for p, u_1, and u_2 in Table 5. It is noteworthy that the errors increase with the increase of t_{final}. It is difficult to determine whether this is due to insufficient network storage space or the accumulation of time-stepping errors. The impact of network architecture on prediction accuracy is discussed in Table 6. It is found that only when the network architecture is less than 2 hidden layers with 32 neurons per layer, will the prediction accuracy of the network be significantly decreased.

To further investigate the impact of blocking variables from participating in gradient backpropagation on accuracy, we examine the effect of increasing the number of variables involved in gradient backpropagation and compare it with the original algorithm. In the original algorithm, only one variable participated in gradient backpropagation during
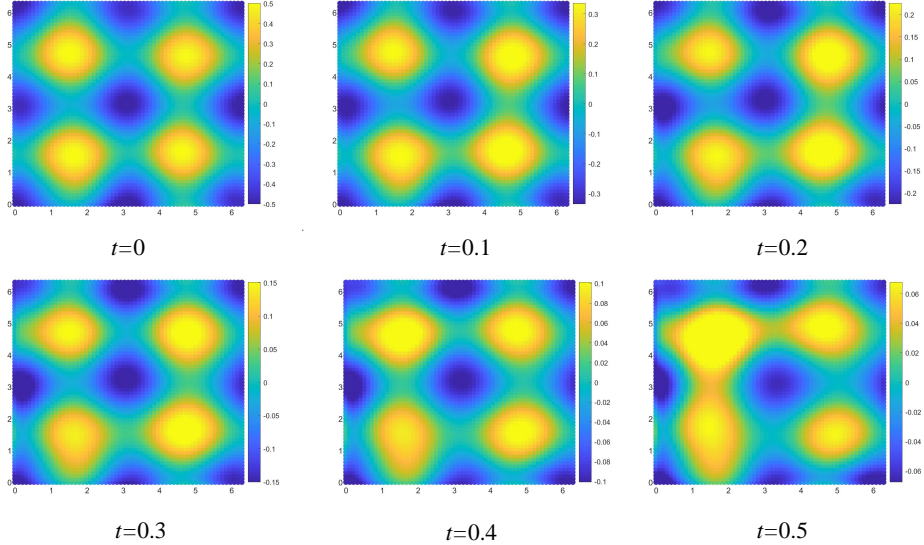
Figure 10: The spatial distribution of p. From left to right is their change with time. Boundary conditions with p. $\Delta t = 0.0125$
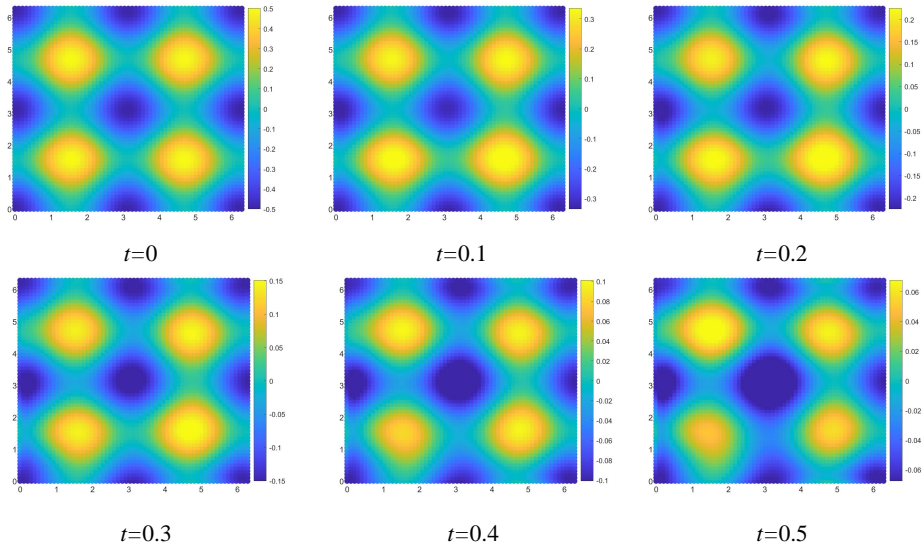

Figure 11: The spatial distribution of p. From left to right is their change with time. Boundary conditions with p. $\Delta t = 0.005$

each step, namely $\frac{\partial^2 p}{\partial xi \partial xi}$ and u_i. We then introduce two additional variables, namely $\frac{\partial p}{\partial xi}$ and $\frac{\partial ui}{\partial x_i}$, and compare the results with the original algorithm. The term "NULL" denotes the original algorithm.

We only consider first-order variables to participate in gradient backpropagation, as involving second-order variables in gradient backpropagation would significantly increase memory usage and reduce computational efficiency.

The effect of the number of variables involved in gradient backpropagation is illustrated in Fig. 12 and summarized in Table 7. From the decline curve of the loss function, it can be observed that the decline speed of the loss function decreases with an increase in the number of variables involved in gradient backpropagation. However, in terms of final

Table 4

Relative final prediction errors of p, u_1 and u_2 measured in the L_2 norm for different time-steps Δt. Sampling interval in space is fixed to $\Delta x_1 = 0.05\pi$ and $\Delta x_2 = 0.05\pi$. The network architecture is 3 hidden layers with 64 neurons per layer.

Parameters \ Δt	0.1	0.05	0.025	0.0125	0.005
p	4.5e-1	3.3e-1	2.5e-1	1.7e-1	1.3e-1
u_1	2.7e-2	2.2e-2	2.0e-2	1.7e-2	6.9e-3
u_2	2.6e-2	2.4e-2	2.0e-2	1.5e-2	7.1e-3

Table 5

Relative final prediction errors of p, u_1 and u_2 measured in the L_2 norm for different total time t_{final}. Sampling interval is fixed to $\Delta x_1 = 0.05\pi$, $\Delta x_2 = 0.05\pi$ and $\Delta t = 0.005$. The network architecture is 3 hidden layers with 64 neurons per layer.

Parameters \ t_{final}	0.1	0.2	0.3	0.4	0.5
p	6.4e-2	9.4e-2	1.1 e-1	1.2e-1	1.3e-1
u_1	2.0e-3	3.0e-3	4.2e-3	5.5e-3	6.9e-3
u_2	2.1e-3	3.4e-3	4.8e-3	6.3e-3	7.1e-3

Table 6

Relative final prediction errors of p, u_1 and u_2 measured in the L_2 norm for different number of hidden layers and neurons per layer. Sampling interval is fixed to $\Delta x_1 = 0.05\pi$, $\Delta x_2 = 0.05\pi$ and $\Delta t = 0.005$.

Relative final prediction errors of p					Relative final prediction errors of u_1			
Layers \ Neurons	16	32	64	128	Layers \ Neurons	16	32	64	128
2	3.0e-1	2.1e-1	1.5e-1	1.4e-1	2	2.9e-2	2.0e-2	8.5e-3	9.5e-3
3	1.7e-1	1.4e-1	1.3e-1	1.3e-1	3	8.7e-3	8.4e-3	6.7e-3	7.6e-3
4	1.4e-1	1.3e-1	1.3e-1	1.3e-1	4	7.0e-3	8.1e-3	7.2e-3	6.9e-3

Relative final prediction errors of u_2				
Layers \ Neurons	16	32	64	128
2	2.1e-2	1.7e-2	8.3e-3	8.7e-3
3	8.9e-3	8.0e-3	7.2e-3	7.5e-3
4	7.7e-3	8.0e-3	7.0e-3	7.1e-3

Table 7

Relative final prediction errors of p, u_1 and u_2 measured in the L_2 norm for different additional parameters involved in gradient backpropagation. Sampling inccerval is fixed to $\Delta x_1 = 0.05\pi$, $\Delta x_2 = 0.05\pi$ and $\Delta t = 0.005$. $t_{final} = 0.2$. The network architecture is 3 hidden layers with 64 neurons per layer.

Parameters	Additional variables			
	NULL	$\frac{\partial p}{\partial x_i}$	$\frac{\partial u_i}{\partial x_i}$	$\frac{\partial p}{\partial x_i}$ and $\frac{\partial u_i}{\partial x_i}$
p	2.12e-1	2.13e-1	2.10e-1	2.12e-1
u_1	7.07e-3	7.06e-3	7.12e-3	7.06e-3
u_2	7.36e-3	7.44e-3	7.42e-2	7.46e-2

accuracy, the additional variables did not have a significant impact on the accuracy of the results. It is not entirely reliable to infer the solution accuracy based solely on the loss function.

Overall, the key parameters that control the performance of our method are the time-step Δt, which is consistent with the conclusion obtained by Raissi et al. (2019) using the Runge-Kutta method.
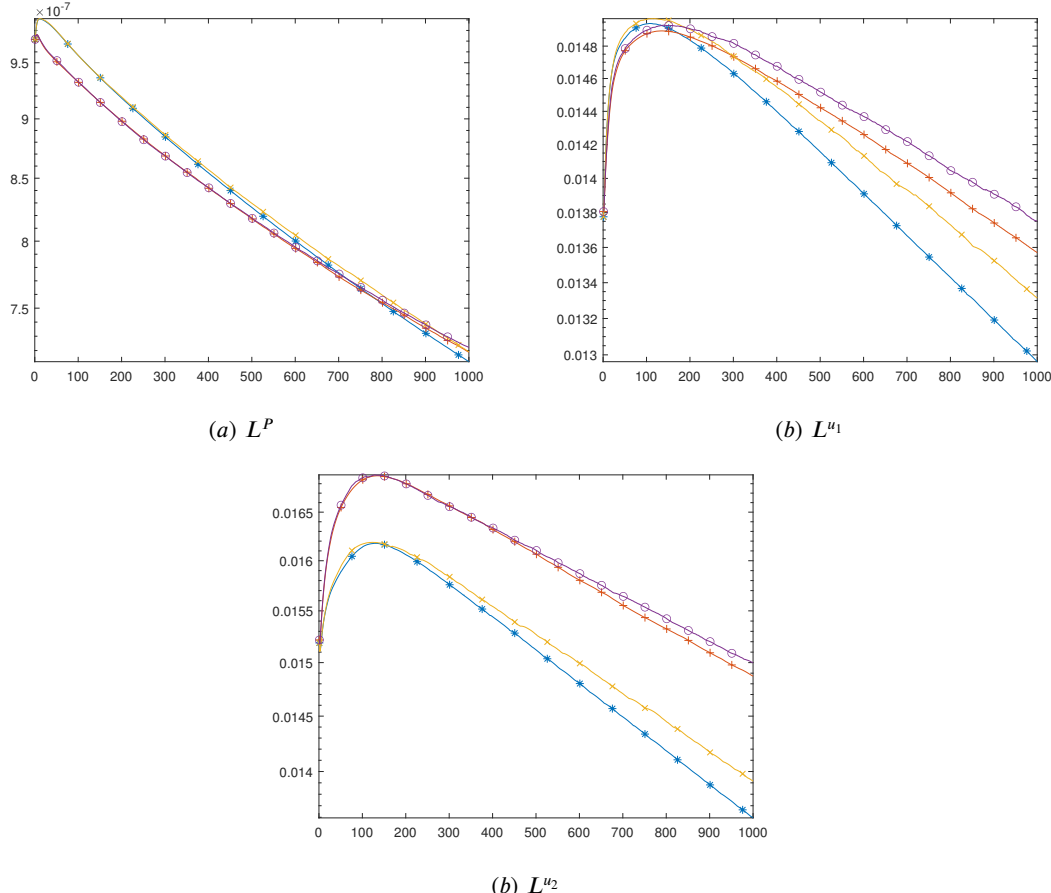
(a) L^P

(b) L^{u_1}

(b) L^{u_2}

Figure 12: The Loss function of the parameter p and u_i changes with the different number of variables involved in gradient backpropagation. $*$ represents the original algorithm. $+$, $\times$ and o represent $\frac{\partial p}{\partial x_i}$, $\frac{\partial u_i}{\partial x_i}$ and $\frac{\partial p}{\partial x_i}$ add $\frac{\partial u_i}{\partial x_i}$, respectively. Sampling inccerval is fixed to $\Delta x_1 = 0.05\pi$, $\Delta x_2 = 0.05\pi$ and $\Delta t = 0.005$. $t_{final} = 0.2$. The network architecture is 3 hidden layers with 64 neurons per layer.

5. Conclusions

This paper presents a PINN method based on CBS that can effectively solve shallow-water equations, making it suitable for ocean flow field estimation. By solving incompressible N-S equations with exact solutions, we prove the correctness and universality of this method. Compared to other methods, our approach is computationally efficient as it does not consider the weights between output parameters, and not all partial derivatives are involved in gradient backpropagation. We investigate the minimum number of conditions required to ensure the reliability and stability of the network output. Our method can provide reliable results even with minimal data volumes. We also discuss the circumstances in which this method requires more stringent conditions than the finite element method. This is mainly due to the partial derivative term in the PINN not being zero at the boundary, which can lead to inaccurate predictions if not taken into consideration.

We compared the effects of network structure, time-step, and gradient backpropagation on the results and found that the network structure is not the primary factor affecting the accuracy, but rather the method itself. In our proposed method, the time-step plays a crucial role in determining the accuracy. Like the finite element method, the neural network is a spatiotemporal approximation method that requires corresponding algorithms to explore its performance fully. Although the solution speed of neural network methods is generally slower than that of traditional methods such as the finite element method, PINN has advantages in scenarios that require processing data for multiple time steps. Traditional numerical methods can only handle data for one time step at a time, which may exhibit limitations as the

amount of data increases. In contrast, PINN can utilize data from multiple time steps simultaneously, demonstrating advantages and in some cases (Bi, Xie, Zhang, Chen, Gu and Tian, 2023), exhibiting faster speed and higher accuracy.

References

Amini Niaki, S., Haghighat, E., Campbell, T., Poursartip, A., Vaziri, R., 2021. Physics-informed neural network for modelling the thermochemical curing process of composite-tool systems during manufacture. Computer Methods in Applied Mechanics and Engineering 384, 113959. URL: https://www.sciencedirect.com/science/article/pii/S0045782521002966, doi:https://doi.org/10.1016/j.cma.2021.113959.

Bandai, T., Ghezzehei, T.A., 2021. Physics-informed neural networks with monotonicity constraints for richardson-richards equation: Estimation of constitutive relationships and soil water flux density from volumetric water content measurements. Water Resources Research 57.

Barreau, M., Aguiar, M., Liu, J., Johansson, K.H., 2021. Physics-informed learning for identification and state reconstruction of traffic density, in: 2021 60th IEEE Conference on Decision and Control (CDC), pp. 2653–2658. doi:10.1109/CDC45484.2021.9683295.

Bi, K., Xie, L., Zhang, H., Chen, X., Gu, X., Tian, Q., 2023. Accurate medium-range global weather forecasting with 3d neural networks. Nature , 1–6.

Chen, Y., Huang, D., Zhang, D., Zeng, J., Wang, N., Zhang, H., Yan, J., 2021. Theory-guided hard constraint projection (hcp): A knowledge-based data-driven scientific machine learning method. Journal of Computational Physics 445, 110624. URL: https://www.sciencedirect.com/science/article/pii/S0021999121005192, doi:https://doi.org/10.1016/j.jcp.2021.110624.

Codina, R., Vázquez, M., Zienkiewicz, O.C., 1998. A general algorithm for compressible and incompressible flows. part iii: The semi-implicit form. International Journal for Numerical Methods in Fluids 27, 13–32.

Dulebenets, M.A., 2021. An adaptive polyploid memetic algorithm for scheduling trucks at a cross-docking terminal. Information Sciences 565, 390–421. URL: https://www.sciencedirect.com/science/article/pii/S002002552100181X, doi:https://doi.org/10.1016/j.ins.2021.02.039.

Dwivedi, V., Srinivasan, B., 2020. Physics informed extreme learning machine (pielm)–a rapid method for the numerical solution of partial differential equations. Neurocomputing 391, 96–118. URL: https://www.sciencedirect.com/science/article/pii/S0925231219318144, doi:https://doi.org/10.1016/j.neucom.2019.12.099.

Ethier, C.R., Steinman, D., 1994. Exact fully 3d navier–stokes solutions for benchmarking. International Journal for Numerical Methods in Fluids 19, 369–375.

F.R.S., G.T., 1923. Lxxv. on the decay of vortices in a viscous fluid. The London, Edinburgh, and Dublin Philosophical Magazine and Journal of Science 46, 671–674. URL: https://doi.org/10.1080/14786442308634295, doi:10.1080/14786442308634295, arXiv:https://doi.org/10.1080/14786442308634295.

Jagtap, A.D., Kawaguchi, K., Karniadakis, G.E., 2020. Adaptive activation functions accelerate convergence in deep and physics-informed neural networks. Journal of Computational Physics 404, 109136.

Kani, J.N., Elsheikh, A.H., 2018. Reduced order modeling of subsurface multiphase flow models using deep residual recurrent neural networks. Transport in Porous Media .

Kavoosi, M., Dulebenets, M.A., Abioye, O., Pasha, J., Theophilus, O., Wang, H., Kampmann, R., Mikijeljević, M., 2019a. Berth scheduling at marine container terminals: A universal island-based metaheuristic approach. Maritime Business Review 5, 30–66.

Kavoosi, M., Dulebenets, M.A., Abioye, O.F., Pasha, J., Wang, H., Chi, H., 2019b. An augmented self-adaptive parameter control in evolutionary computation: A case study for the berth scheduling problem. Advanced Engineering Informatics 42, 100972. URL: https://www.sciencedirect.com/science/article/pii/S1474034619305452, doi:https://doi.org/10.1016/j.aei.2019.100972.

Liu, D., Wang, Y., 2019. Multi-fidelity physics-constrained neural network and its application in materials modeling. Journal of mechanical design , 141.

Liu, Z., Cai, W., Xu, Z.Q.J., 2020. Multi-scale deep neural network (mscalednn) for solving poisson-boltzmann equation in complex domains. Communications in Computational Physics 28.

Löhner, R., Morgan, K., Zienkiewicz, O.C., 1984. The solution of non-linear hyperbolic equation systems by the finite element method. International Journal for Numerical Methods in Fluids 4, 1043–1063.

Long, Z., Lu, Y., Dong, B., 2019. Pde-net 2.0: Learning pdes from data with a numeric-symbolic hybrid deep network. Journal of Computational Physics 399, 108925.

Long, Z., Lu, Y., Ma, X., Dong, B., 2018. Pde-net: Learning pdes from data, in: International Conference on Machine Learning, PMLR. pp. 3208–3216.

Lyu, L., Zhang, Z., Chen, M., Chen, J., 2022. Mim: A deep mixed residual method for solving high-order partial differential equations. Journal of Computational Physics 452, 110930.

Mao, Z., Jagtap, A.D., Karniadakis, G.E., 2020. Physics-informed neural networks for high-speed flows. Computer Methods in Applied Mechanics and Engineering 360, 112789. URL: https://www.sciencedirect.com/science/article/pii/S0045782519306814, doi:https://doi.org/10.1016/j.cma.2019.112789.

Pasha, J., Nwodu, A.L., Fathollahi-Fard, A.M., Tian, G., Li, Z., Wang, H., Dulebenets, M.A., 2022. Exact and metaheuristic algorithms for the vehicle routing problem with a factory-in-a-box in multi-objective settings. Advanced Engineering Informatics 52, 101623. URL: https://www.sciencedirect.com/science/article/pii/S1474034622000891, doi:https://doi.org/10.1016/j.aei.2022.101623.

Rabbani, M., Oladzad-Abbasabady, N., Akbarian-Saravi, N., 2022. Ambulance routing in disaster response considering variable patient condition: Nsga-ii and mopso algorithms. Journal of Industrial and Management Optimization 18, 1035–1062.

Raissi, M., Perdikaris, P., Karniadakis, G., 2019. Physics-informed neural networks: A deep learning framework for solving forward and inverse problems involving nonlinear partial differential equations. Journal of Computational Physics 378, 686–707. URL: https://www.sciencedirect.com/science/article/pii/S0021999118307125, doi:https://doi.org/10.1016/j.jcp.2018.10.045.

Raissi, M., Perdikaris, P., Karniadakis, G.E., 2017a. Physics informed deep learning (part i): Data-driven solutions of nonlinear partial differential equations. arXiv preprint arXiv:1711.10561 .

Raissi, M., Perdikaris, P., Karniadakis, G.E., 2017b. Physics informed deep learning (part ii): Data-driven discovery of nonlinear partial differential equations. arXiv preprint arXiv:1711.10566 .

Raissi, M., Yazdani, A., Karniadakis, G.E., 2020. Hidden fluid mechanics: Learning velocity and pressure fields from flow visualizations. Science 367, 1026–1030.

Ranade, R., Hill, C., Pathak, J., 2021. Discretizationnet: A machine-learning based solver for navier–stokes equations using finite volume discretization. Computer Methods in Applied Mechanics and Engineering 378, 113722. URL: https://www.sciencedirect.com/science/article/pii/S004578252100058X, doi:https://doi.org/10.1016/j.cma.2021.113722.

Schiassi, E., D'Ambrosio, A., Drozd, K., Curti, F., Furfaro, R., 2022. Physics-informed neural networks for optimal planar orbit transfers. Journal of Spacecraft and Rockets 59, 834–849.

Shankar, P.N., Deshpande, M., 2000. Fluid mechanics in the driven cavity. Annual Review of Fluid Mechanics 32.

Snaiki, R., 2019. Knowledge-enhanced deep learning for simulation of tropical cyclone boundary-layer winds. Journal of Wind Engineering and Industrial Aerodynamics: The Journal of the International Association for Wind Engineering 194.

Wang, B., Zhang, W., Cai, W., 2020. Multi-scale deep neural network (mscalednn) methods for oscillatory stokes flows in complex domains. Communications in Computational Physics 28, 2139–2157.

Wang, H., Liu, Y., Wang, S., 2022. Dense velocity reconstruction from particle image velocimetry/particle tracking velocimetry using a physics-informed neural network. Physics of fluids , 34.

Wang, S., Wang, H., Perdikaris, P., 2021. On the eigenvector bias of fourier feature networks: From regression to solving multi-scale pdes with physics-informed neural networks. Computer Methods in Applied Mechanics and Engineering 384, 113938. URL: https://www.sciencedirect.com/science/article/pii/S0045782521002759, doi:https://doi.org/10.1016/j.cma.2021.113938.

Xu, Z., Zhang, Y., Luo, T., Xiao, Y., Ma, Z., 2020. Frequency principle: Fourier analysis sheds light on deep neural networks. Communications in Computational Physics .

Xu, Z.Q.J., Zhang, Y., Xiao, Y., 2019. Training behavior of deep neural network in frequency domain, in: Gedeon, T., Wong, K.W., Lee, M. (Eds.), Neural Information Processing, Springer International Publishing, Cham. pp. 264–274.

Yang, L., Meng, X., Karniadakis, G.E., 2021. B-pinns: Bayesian physics-informed neural networks for forward and inverse pde problems with noisy data. Journal of Computational Physics 425, 109913. URL: https://www.sciencedirect.com/science/article/pii/S0021999120306872, doi:https://doi.org/10.1016/j.jcp.2020.109913.

Zhao, H., Zhang, C., 2020. An online-learning-based evolutionary many-objective algorithm. Information Sciences 509, 1–21. URL: https://www.sciencedirect.com/science/article/pii/S0020025519308187, doi:https://doi.org/10.1016/j.ins.2019.08.069.

Zienkiewicz, O., Taylor, R., Nithiarasu, P. (Eds.), 2014. The Characteristic-Based Split (CBS) Algorithm. seventh edition ed.. Butterworth-Heinemann, Oxford. pp. 87–118. URL: https://www.sciencedirect.com/science/article/pii/B9781856176354000340, doi:https://doi.org/10.1016/C2009-0-26328-8.